RESEARCH ARTICLE
Cytoskeleton, January 2017 74:3–17 (doi: 10.1002/cm.21346)


# Modeling the Effects of Lattice Defects on Microtubule Breaking and Healing

Nan Jiang,[1] Megan E. Bailey,[2] Jessica Burke,[1] Jennifer L. Ross,[2,3] and Ruxandra I. Dima[1]*

[1]Department of Chemistry, University of Cincinnati, Cincinnati, Ohio 45221
[2]Molecular and Cellular Biology Graduate Program, University of Massachusetts Amherst, Amherst, Massachusetts 01003
[3]Department of Physics, University of Massachusetts Amherst, Amherst, Massachusetts 01003

Received 2 November 2016; Revised 29 November 2016; Accepted 29 November 2016
Monitoring Editor: Manuel Théry

**Microtubule reorganization often results from the loss of polymer induced through breakage or active destruction by energy-using enzymes. Pre-existing defects in the microtubule lattice likely lower structural integrity and aid filament destruction. Using large-scale molecular simulations, we model diverse microtubule fragments under forces generated at specific positions to locally crush the filament. We show that lattices with 2% defects are crushed and severed by forces three times smaller than defect-free ones. We validate our results with direct comparisons of microtubule kinking angles during severing. We find a high statistical correlation between the angle distributions from experiments and simulations indicating that they sample the same population of structures. Our simulations also indicate that the mechanical environment of the filament affects breaking: local mechanical support inhibits healing after severing, especially in the case of filaments with defects. These results recall reports of microtubule healing after flow-induced bending and corroborate prior experimental studies that show severing is more likely at locations where microtubules crossover in networks. Our results shed new light on mechanisms underlying the ability of microtubules to be destroyed and healed in the cell, either by external forces or by severing enzymes wedging dimers apart.** © 2016 Wiley Periodicals, Inc.

**Key Words:** microtubule mechanics; coarse-grained simulations; microtubule severing enzymes; atomic force spectroscopy; katanin; spastin

Additional Supporting Information may be found in the online version of this article.

*Address correspondence to: Ruxandra I. Dima, Department of Chemistry, University of Cincinnati, Cincinnati, Ohio 45221. E-mail: dimari@ucmail.uc.edu

Published online 9 December 2016 in Wiley Online Library (wileyonlinelibrary.com).

## Introduction

Microtubules (MTs) are the structural backbone of the cell responsible for cell morphology, interior organization, and intracellular cargo transport of macromolecules and organelles. In this role, the MT network must have the ability to dynamically organize and rearrange for essential processes such as cell division, cell motility, and cell development [Nogales et al., 1998; Johnson et al., 2007; Paul et al., 2008; Sharp & Ross, 2012]. Much attention has been paid to MT dynamic instability, the intrinsic, stochastic polymerization-depolymerization dynamics that MTs display. But, there are other mechanisms of MT reorganization and reorientation at work in cells. Two biologically relevant mechanisms of MT breakage have been observed in cells: breaking from high frequency buckling of filaments and breaking induced by microtubule-severing enzymes [Waterman-Storer & Salmon, 1997; Ahmad et al., 1999; Brangwynne et al., 2006]. Both types of breakage activities lead to loss of tubulin dimer subunits within the lattice to create defects.

A newly published paper demonstrated that the link between lattice defects and MT healing is likely an important regulatory mechanism for reshaping, remodeling, and strengthening the MT cytoskeletal network [Aumeier et al., 2016]. Using a laser, the authors locally damaged MTs and showed that, in live cells, the resulting MTs were patched and healed by the addition of new dimers and those healed sites corresponded to rescue sites during dynamic instability implying they had altered dimer structure and mechanical properties. If enough damage occurred in a particular region of MTs, the enhanced mechanical robustness of the healed filaments could cause a build up of MTs in that region and even change the direction of growth and motility of the cell [Aumeier et al., 2016].

In vitro, MT lattice defects are known to occur with a higher frequency when MTs are polymerized quicker [Dogterom & Yurke, 1997; Schaedel et al., 2015]. Prior work using aqueous AFM on defect-free Taxol-stabilized

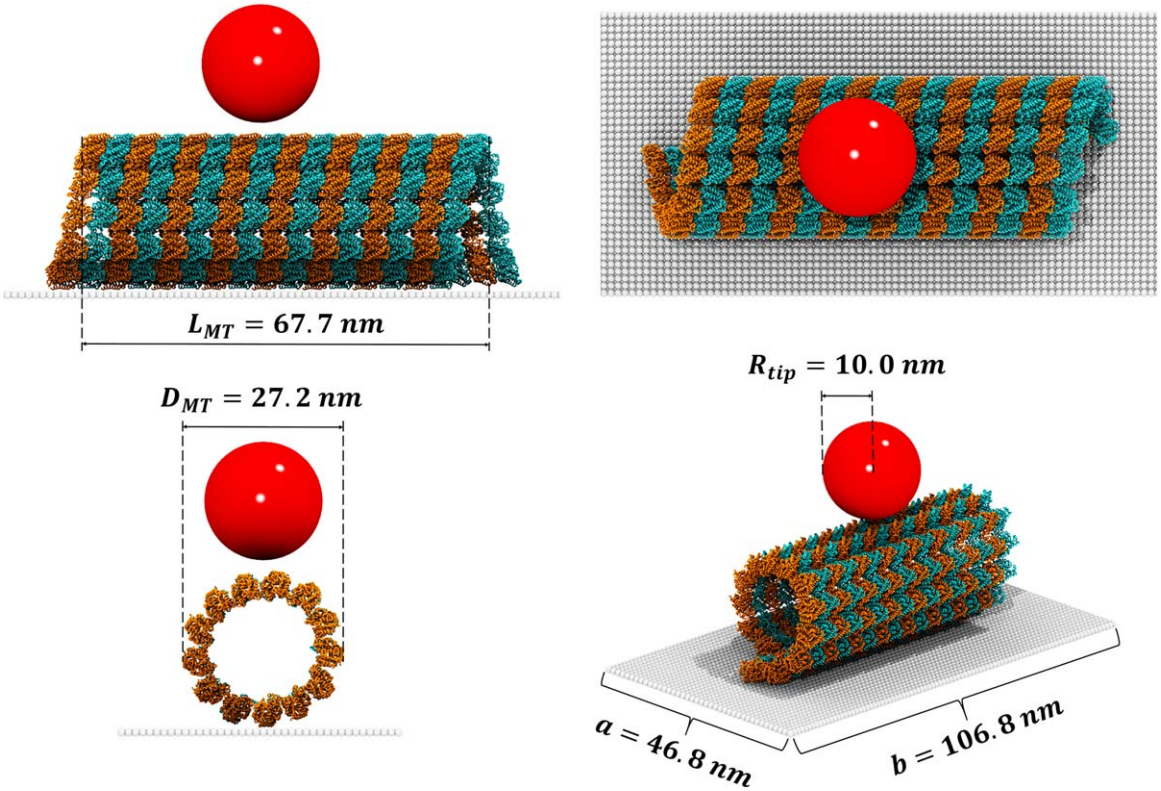


**Fig. 1. The MT model and the indentation setup.** Our MT model with 8 dimers per PF and the indentation setup are shown from different perspectives: side view (top left inset), minus end front view (bottom left inset), top view (top right inset) and oblique orthogonal view (bottom right inset). The α monomers are orange and the β monomers are cyan, a color convention used in all conformational snapshots. These and all the other structural renderings of the complex were done using visual molecular dynamics (VMD) [Humphrey et al., 1996] and Povray programs. [Color figure can be viewed at wileyonlinelibrary.com]

MTs has shown that the AFM could remove a single dimer by pushing on the lattice directly [de Pablo et al., 2003; Schaap et al., 2004, 2006]. The removed dimer could reseal and heal or cause complete collapse, depending on the extent of the initial damage [de Pablo et al., 2003; Schaap et al., 2004, 2006]. Additionally, a recent study showed that MTs are mechanically softer when defects occur [Schaedel et al., 2015]. Interestingly, these defects could heal when MTs were incubated with free tubulin dimers and healing enabled the recovery of MT stiffness [Schaedel et al., 2015]. We have previously shown that severing enzymes have higher affinity for defect sites within the filament [Díaz-Valencia et al., 2011], which verified an earlier model suggesting that severing occurred most likely at defect sites [Davis et al., 2002]. Overall, these prior works paint a picture that the mechanical and dynamic nature of MTs is intimately linked with the local, nanoscale structural integrity of the filament. Further, the filament structure and mechanics has direct implications for the network integrity, density, and location over time.

Since direct experimental measurements of force at the nanoscale are difficult, we have implemented a computational approach to address the question of MT breaking. Computational studies of biomolecular ensembles require the use of enhanced sampling techniques such as replica exchange, metadynamics, or accelerated dynamics with atomistic molecular dynamics simulations, which provide thermodynamic insight into their conformational landscape [Scarabelli & Grant, 2013; Maximova et al., 2016], and of stochastic models, which can be used to determine rates of conversion between states [Wei et al., 2016]. Moreover, limitations in the lengthscale and timescale inherent to all-atomic description call for the use of computationally-intensive, coarse-grained approaches that can provide both statistically significant and experimentally relevant information about the conformational changes in large-size biomolecular assemblies such as MTs [Chu & Voth, 2006; Zhou et al., 2007; Feig & Sugita, 2013]. One such model is the self-organized polymer model (SOP-model) [Hyeon et al., 2006a], which allows us to use experimental values of pulling speed to describe the force-induced unfolding reactions in proteins in experimental centisecond time. The SOP model led to insight into the micromechanics of MT protofilaments (PFs), fibrinogen tandems, and virus capsids in agreement with experimental measurements [Zhmurov et al., 2011; Theisen et al., 2012; Kononova et al., 2013; Theisen et al., 2013]. Furthermore, we have successfully employed this model to understand the mechanical control of molecular motors [Hyeon & Onuchic, 2007; Zhang & Thirumalai, 2012], the details of large scale allosteric

**Table I. Collapse Forces. Comparison of Forces for Collapse in Defect-free MTs and MTs with Defects**

| Lattice | First break force/nN | Critical force/nN |
|---|---|---|
| Defect-free | 0.498 ± 0.077 | 0.752 ± 0.111 |
| Defects under tip | 0.287 ± 0.097 | 0.532 ± 0.087 |

transformations in GroEL [Hyeon et al., 2006b], and the folding steps for denatured proteins [Liu et al., 2011; Reddy et al., 2012]. Previously, when running indentation trajectories using the SOP-GPU program [Zhmurov et al., 2010] for a 13 PFs MT filament in a GDP-like state, we found close agreement with forces measured in experimental studies [de Pablo et al., 2003; Schaap et al., 2006] and provided estimates for the free energies of dissociation of the lateral and longitudinal interfaces in the lattice [Kononova et al., 2014].

Here, we used our approach [Kononova et al., 2014], which describes the tubulin subunits at amino acid-level, applied to various MT lattices and combined with force generation at specific positions akin to AFM indentation experiments (Fig. 1) to explore how the MT can be destroyed at the molecular level. Defects in the MT lattice have been repeatedly linked with the action of severing proteins, especially because they are believed to alter the mechanical properties of the filament. While the work reviewed above [Schaedel et al., 2015] confirmed that preexisting defects in a MT lattice lead to lower filament stiffness, the molecular transitions responsible for this behavior and the range of forces required to induce lattice breaking are unknown. Furthermore, experiments are inherently low-precision and random in how they apply forces to measure mechanics and the level of defects in the lattice. In order to understand how the location of the force on the MT structure can lead to filament breakage, new simulations are needed. Here, we addressed these gaps in knowledge through simulations of MT lattices with defects, which, to the best of our knowledge, represent the first time that molecular simulations have been used to study systematically the mechanical response of such lattices. Moreover, we also investigated the effect that constraints placed on the lattice have on the breaking and recovery processes, which is also new.

Finally, given the biological relevance of MT healing for MT rescue during dynamic instability and the network remodeling directly resultant from that [Aumeier et al., 2016], we investigated the ability of the filament to heal after indentation. We compare our simulations to published and new experimental results and find surprisingly good agreement. Our work reveals new insights about the MT stability, the role of lattice defects in the micromechanics of filaments, and the mechanism of crushing MTs, which could be employed by severing enzymes to tear MTs apart. We find that the most damage is done when the MT wall is pushed apart, especially in lattices with 2% defects consisting of subunit vacancies from neighboring PFs, which gives new credence to the wedge model for lattice breaking during MT severing, when previous results had pointed to the unfoldase mechanism for severing.

## Results

### Force Response of Defect-Free Filaments Versus Filaments with Defects

We sought to determine how lattice detects affect the mechanical nature of MTs. Specifically, we pushed on MT filaments that were either defect-free or had lattice defects in the form of missing dimers. Because the simulation has control over many variables, including molecular-scale control over the MT structure and interactions, we made different types of MTs to push on. The numbering of the subunits in a MT lattice is in Supporting Information Fig. S1. The different types of MT structures we tried include a regular lattice (GDP-lattice), a regular lattice with enhanced interactions between protofilaments 5 and 6 ("PF5-PF6"), a laterally homogeneous MT (LHM) model where all lateral interfaces are adjusted to the same total energy value, and an all homogeneous MT (AHM) model in which, on top of the condition for LHM, all the longitudinal interactions are set to the average energy per longitudinal interface. LHM and AHM lattices could be stand ins for the GTP (or GMPCPP)-like state of a MT. Each of these types of lattices could have zero to 2% defects. For more specific information, please see the Methods section.

Our simulations show that the force needed to break the MT structure decreased as the percentage of defects in the lattice increased. The highest breaking force was required by the defect-free lattice with strong lateral contacts, while the lowest force corresponded to the lattice with 2% defects (2 missing dimers). Namely, the most probable force leading to the first breaking event for the defect-free lattice is ∼ 500 pN, while lattices with defects located under the cantilever tip require only 50% of this force value (Table I, Supporting Information Tables S1–S3, and Supporting Information Fig. S4). Similarly, the most probable critical force for the defect-free lattice is ∼ 750 pN, while for the lattices with defects located under the cantilever tip, this is reduced to ∼ 500 pN (a 32% reduction in magnitude, Figs. 2 and 3, Table I and Supporting Information Tables S1–S3). Importantly, we found that lattices with defects located far away (2 or 3 PFs away) from the indentation area break under the same forces as the defect-free regular lattice (see entries "Dimer 43, Dimer 49, and Dimer 52" in Supporting Information Table S2).

In agreement with our previous work [Kononova et al., 2014], our results for the regular lattice, a mimic for the

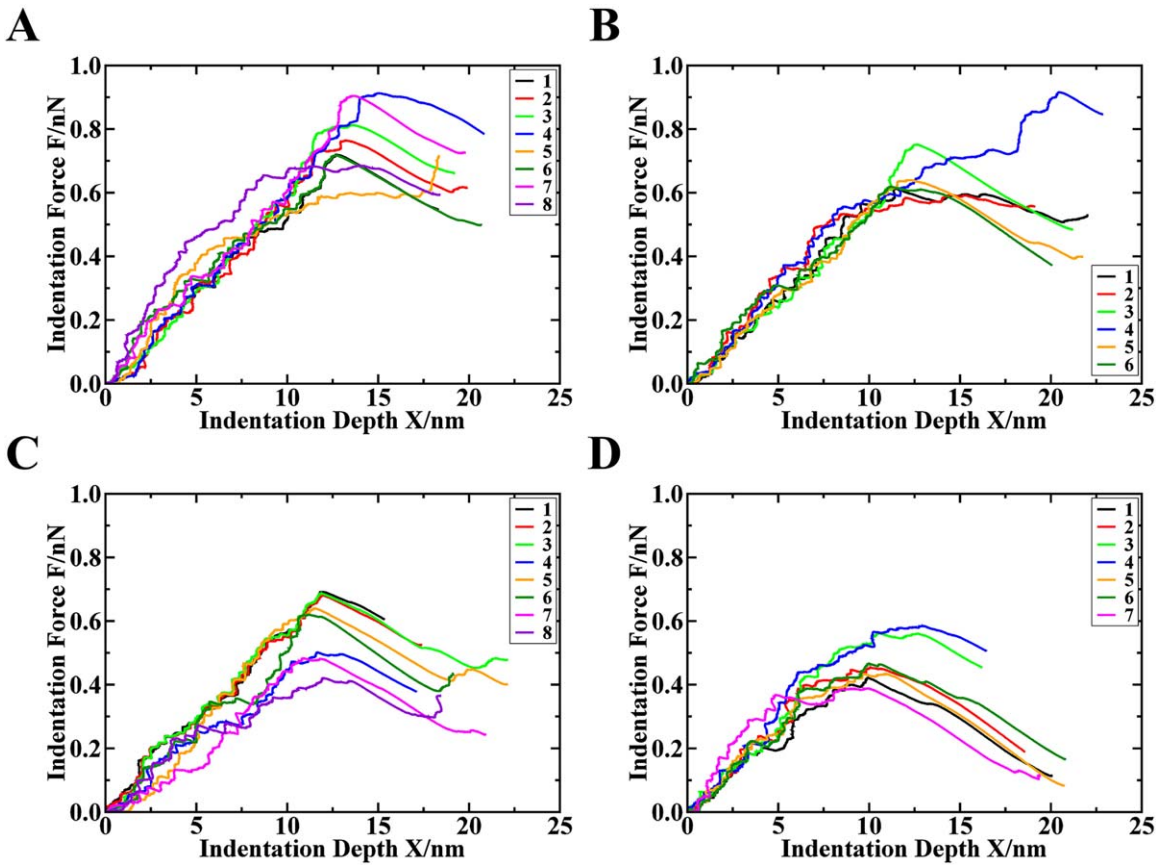


**Fig. 2. Force versus indentation depth curves for MT lattices indented in the middle of the filament.** (A): Defect-free MT lattices pushed between PFs. 1. Regular with both ends fixed with plane. 2. AHM with both ends fixed with plane. 3. LHM with both ends fixed with plane. 4. PF5-PF6 enhanced with both ends fixed with plane. 5. Regular with plus end free with plane. 6. Regular with both ends fixed without plane. 7. AHM with both ends fixed without plane. 8. AHM with plus end free without plane. (B): Defect-free MT lattices pushed on a PF. 1. Regular with both ends fixed with plane pushed on PF6. 2. Regular with plus end free with plane pushed on PF6. 3. Regular with both ends fixed with plane pushed on PF7. 4. Regular with plus end free with plane pushed on PF7. 5. AHM with both ends fixed with plane pushed on PF6. 6. AHM with both ends fixed without plane pushed on PF6. (C): MT lattices with defects pushed between PFs. 1. Missing dimer 43. 2. Missing dimer 49. 3. Missing dimer 52. 4. Missing dimer 45. 5. Missing dimer 46. 6. Missing dimer 47. 7. Missing dimers 45,58. 8. Missing dimers 58,59. (D): Lattice with defects pushed on a PF. 1. Missing dimer 45 pushed on α monomer. 2. Missing dimer 45 pushed on β monomer. 3. Missing dimer 46 pushed on α monomer. 4. Missing dimer 46 pushed on β monomer. 5. Missing dimers 45,58 pushed on α monomer. 6. Missing dimers 45,58 pushed on β monomer. 7. Missing dimers 58,59 pushed on α monomer. [Color figure can be viewed at wileyonlinelibrary.com]

GDP state, showed breakage forces between 580 pN and 750 pN (Supporting Information Table S1). For comparison, the critical forces measured by dePablo et al. in their AFM experiments on GDP MTs with Taxol (Fig. 1 from [de Pablo et al., 2003]) are in the 250 pN to 600 pN interval.

We can compare the different types of lattices we simulated. As expected, we found that the highest force was required by the defect-free lattice with strong lateral contacts ("PF5-PF6" in Supporting Information Table S1) when pushing between PFs (∼ 950 pN), while the lowest force corresponded to a lattice with two missing dimers in lateral neighboring PFs ("Dimers 58,59" in Supporting Information Table S2) when pushed between PFs (∼ 370 pN). When pushing on a PF, the lattice with the strongest lateral interfaces required ∼ 800 pN critical force to collapse. Lattices with two missing dimers, which are longitudinal neighbors in a PF ("Dimers 45,58" in Supporting Information Table S2), resist to forces up to 510 pN when pushed between PFs and 460 pN when pushed on a PF. Therefore, in general, MT lattices are more resistant to force when pushed between PFs than when pushed on a PF, in agreement with experiments [Schaap et al., 2006].

Another important finding is that the highest critical force (950 pN) corresponds to the indentation between PFs of an enhanced lateral MT ("PF5-PF6") with both ends fixed (Fig. 2 and Supporting Information Table S1). And the laterally homogeneous MT (LHM) filament requires the next largest average critical force value of 830 pN for

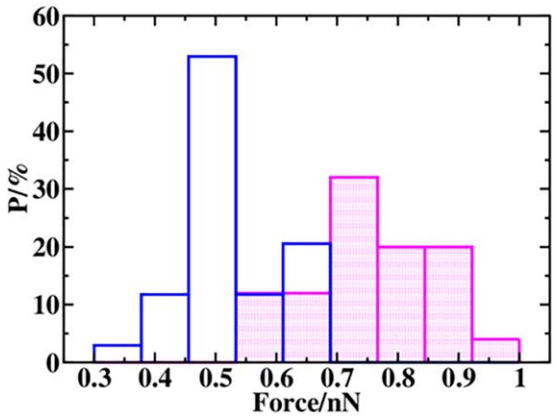


**Fig. 3. Distributions of rupture forces.** Rupture force distribution for defect-free MTs (magenta, 25 points) and MTs with defects under the tip (blue, 34 points). [Color figure can be viewed at wileyonlinelibrary.com]

collapse (Supporting Information Table S1). These forces recapitulate the values obtained for GMPCPP MTs in AFM experiments (Fig. 2 in [Donhauser et al., 2010]), thus providing support for our assumption that a lattice with homogeneous strong lateral contacts is in a GTP-like state. In contrast, the all homogeneous MT (AHM) lattices do not show any further increase in the average breaking force. Thus, our results indicate that the stability of the lateral interactions between PFs is the primary source of mechanical strength in a MT filament.

### The Mechanism of Collapse of MT Filaments Depends on the Strength of Interactions Between Subunits and on Lattice Constraints

A major advantage of our simulations is that we have direct access to the atomic coordinates of all the peptide residues for the duration of each trajectory, which enables us to describe breaking pathways in detail. Figure 4 and Supporting Information Figs. S5 and S6 show that all MT lattices exhibited similar initial deformations (the second step in all panels) corresponding to bending and buckling. This behavior, at a distance, X, between 6 and 8 nm, seen in Fig. 4 for the indentation of the regular MT lattice with both ends fixed (also depicted as top view in Supporting Information Fig. S5A), proves that MTs can sustain low forces loaded on the lattice through deformation and propagation of the compression from the loading position onto a larger area of the filament [Kononova et al., 2014]. Eventually, the force increases such that the lattice can no longer bear the loading force simply by deformation leading to lattice breaking. Differences in the breaking pattern lead to four different pathways, listed in Supporting Information Tables S1–S3 for each run.

The most probable pathway (P1), the same as in our previous work [Kononova et al., 2014], was observed in 16% of the defect-free lattice trajectories and in all trajectories for lattices with defects. Here, we found an initial fracture of lateral contacts between the central PF and one of its neighbors in the lattice, finally leading to the simultaneous breakage of longitudinal and lateral contacts for a set of 3 PFs located on the upper surface of the MT (fourth panel in Supporting Information Fig. S5A and Fig. 4).

The second pathway (P2), found in 64% of all defect-free lattice trajectories, corresponds for example to the indentation between PFs of the enhanced lateral MT ("PF5-PF6" filament) with both ends fixed from Supporting Information Movie S1. In this pathway, lattice rupture initiates with the breakage of one of the longitudinal interfaces connecting the dimer under the sphere with its neighbors along the PF (Supporting Information Fig. S5C). Shortly afterwards, there is substantial fracture of the lateral

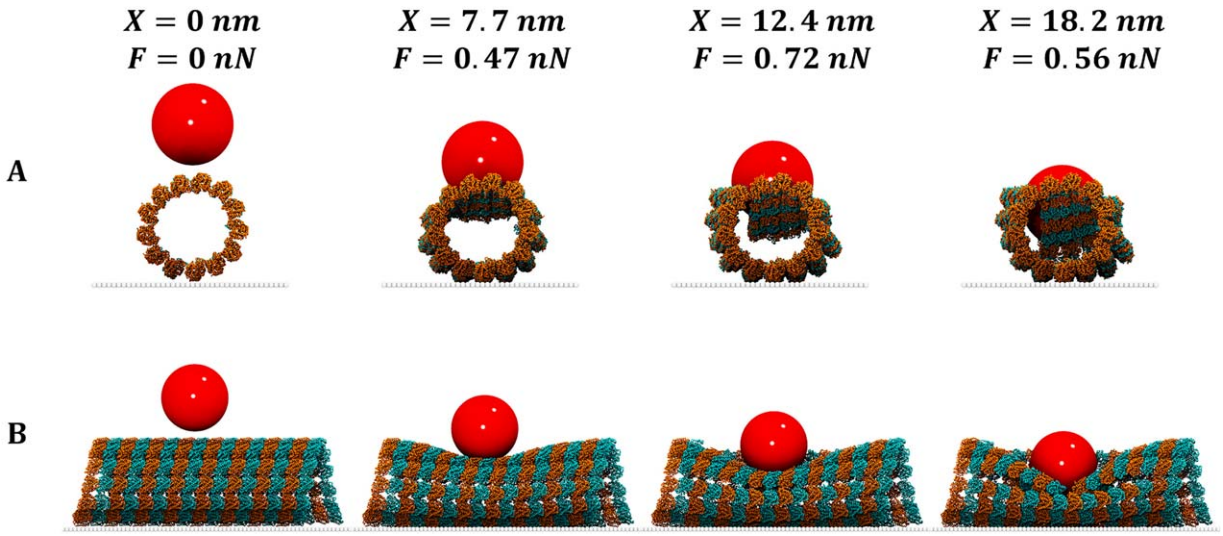


**Fig. 4. Indentation pathway of the defect-free regular MT lattice with both ends fixed pushed between PFs.** The figures correspond in order, from left to right, to the states: initial, first breakage, critical force break, and final state. (A): front view. (B): side view. See also Supporting Information Fig. S5A. [Color figure can be viewed at wileyonlinelibrary.com]

interfaces between the central PF and its neighbors in the lattice and of additional longitudinal interfaces leading to a catastrophic breakdown of the MT (Supporting Information Fig. S5C).

The third pathway (P3), found in 16% of the defect-free lattice trajectories, corresponds to the indentation of the regular lattice between PFs and with the plus end free, as seen in Supporting Information Movie S2. In this case, we found only the fracture of lateral interfaces between 5 of the 8 dimers in two adjacent PFs located under the indentation sphere (PF5 and PF6 in Supporting Information Fig. S1), which requires a low critical force of $\sim$ 580 pN for the 8 dimers long MT (Supporting Information Fig. S5B and Fig. 2A) and $\sim$ 500 pN for the 12 dimers long MT (Supporting Information Fig. S7). Moreover, we found that, following the lateral contacts fracture, there is an overall translation by approximately the length of a dimer (8 nm) of the top PFs from the plus end toward the center of the fragment. The PF slips longitudinally by one lattice spacing. Finally, pushing at the free plus end of the 12 dimers MT leads only to the breaking of lateral contacts, without the PF translation, under an even lower critical force of $\sim$ 320 pN (Supporting Information Fig. S7).

Schaap et al. [Schaap et al., 2006] pushed an MT at different locations starting from the free plus end. They found that the critical force increases with the distance from the plus end up until a distance of 40 nm, where it reaches a plateau (Fig. 3 in [Schaap et al., 2006]). The ratio of the plateau value versus the one at the plus end was 1.9. In our 12 dimers long lattice, we found a similar steady increase in the critical force with the distance from the end (Supporting Information Fig. S7) leading to a corresponding ratio of 1.7. Importantly, because the 50% increase in the length of the MT fragment (from 8 to 12 dimers) leads to only a modest 14% change (decrease) in the critical pushing force, with no change in the indentation pathway, the results for the 8 dimers long filament simulations are likely a good description of the mechanical properties of MTs.

Finally, pathway 4 (P4), found in 4% of the defect-free lattice trajectories, corresponds to the indentation of the regular lattice on PF7 with plus end free (blue line in Fig. 2B). This led to the highest critical force value (920 pN) among all runs where we pushed on a PF, as well as a much larger value of X critical ($\sim$ 20 nm) compared to the typical value (11-15 nm). The pathway corresponds to first breaking lateral interfaces between side PFs close to the fixed minus end of the filament. This is followed by the breaking of longitudinal interfaces in all the PFs on the upper surface of the MT, which occurs at the plateau force of $\sim$ 700 pN (blue line in Fig. 2B) and lasts up to an indentation depth of 18 nm. The peak centered at 20 nm represents the breaking of lateral interfaces between fragments of PF5 and PF6.

All lattices with defects followed the major pathway, P1. However, there were slight differences, depending on whether we pushed between PFs or on a PF. We denoted these variations with P11 and, respectively, P12 in Supporting Information Tables S2 and S3. For example, for the lattice with 2 longitudinal dimers missing ("Dimers 45,58" in Supporting Information Table S2), pushing between PFs showed breaking of a large area around the original indentation region (2 or 3 longitudinal interfaces and up to 2 lateral interfaces), corresponding to scenario P11. In contrast, pushing on a PF led to the breaking of only the specific area where compression was applied (1 lateral and 1 longitudinal interface), corresponding to scenario P12. We found a similar behavior for the lattices with a single vacancy, i.e., when pushing between PFs two (for dimer 45 missing) or three (for dimer 46 missing) longitudinal interfaces broke, while pushing on a PF led to only one (for dimer 45 missing) or two (for dimer 46 missing) longitudinal interfaces broken. Thus, pushing on a PF in lattices with vacancies generates only localized breaking of interfaces, indicating that the lattice is able to easily disperse the applied tension without further substantial loss of subunits. In contrast, when pushing between PFs the lattice is unable to resist force resulting in widespread damage.

### Agreement of Distributions of Kinking Angles Between Simulations and in Vitro Experiments

To further test our model, we compared the angles we find for local distortions of the MT lattice to experiment. The procedure to extract the kinking angle from simulations is described in Section I.4 from the Supporting Information and illustrated in Supporting Information Fig. S2. We chose to compare them to the measurement of MT kinking angles between two intact pieces of MT that are fluctuating during the action of the MT severing enzyme katanin. The kinking angle has been previously measured for katanin [Davis et al., 2002] and compared to theoretical modeling of MT mechanics [Mohrbach & Kulić, 2007]. We demonstrate the kinking experiment and a cartoon illustration in the Supporting Information Fig. S3. In the case of the experiment, katanin is used to remove a portion of the MT lattice to allow it to thermally fluctuate causing the kinking we observe. Thus, the bending is thermally driven and the bending of only a few PFs is occurring. This is similar to our simulations where, due to support from the underlying substrate, only a few PFs are deformed by the outside probe.

We made kinking measurements for two different katanin concentrations, 50 nM and 100 nM. We showed previously that 50 nM and 100 nM katanin had significantly different times to sever [Bailey et al., 2015]. Following the trends reported previously, we find that 50 nM katanin creates lower kinking angles than 100 nM [Davis et al., 2002]. Thus, we posit that the difference between our 50 nM and 100 nM data are a reflection of the speed of the severing process as a function of enzyme concentration. In particular, the MT filament takes longer to sever at the lower

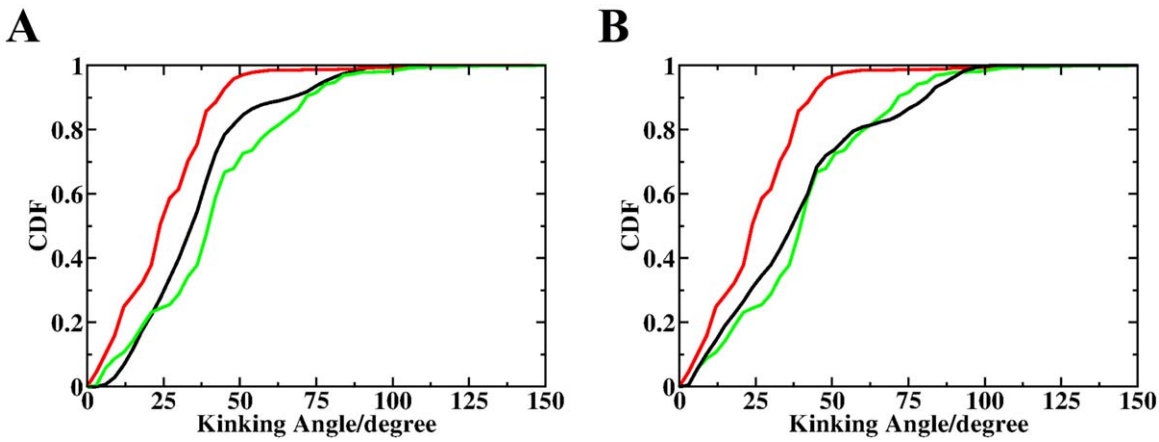


**Fig. 5. Cumulative distribution function of the kinking angles for MTs in simulations and in vitro experiments (from Supporting Information Fig. S3).** The actual distributions are in Fig. S8. In all plots the experimental data for 50 nM katanin is in red and for 100 nM katanin is in green, while the simulation data is in black. The number of data points is: 558 for experiment (50 nM), 822 for experiment (100 nM), 6113 for simulation in (A), and 1300 for simulation in (B). (A): All simulation and the experimental data. The K-S statistical similarity test shows that the simulation data is most similar to the 100 nM experimental data ($D_{crit} = 0.246$, $D$(sims,50 nM) = 0.249 and $D$(sims,100 nM) = 0.167); (B): The simulation data for MTs with 2% defects and both ends fixed and all the experimental data. The K-S statistical similarity test shows that the simulation data is very similar to the 100 nM experimental data ($D$(sims,50 nM) = 0.315 and $D$(sims,100 nM) = 0.104). [Color figure can be viewed at wileyonlinelibrary.com]

katanin-p60 concentration, thus spending longer time in close to native states. This is reflected in the less spread in the angle distribution for the 50 nM compared to the 100 nM case (compare Supporting Information Fig. S3B,C).

The high statistical relatedness between the simulated and experimental angles (Fig. 5) indicates that they sample similar angle distributions. At first glance it might be surprising to find such close similarity between simulation and experimental data that is not exactly the same physical situation of the simulation, but we conclude that the mechanical nature of the intact sheet of PFs fluctuating in experiments is similar to what is simulated. This makes sense, since we see that only the PFs on the top surface are deformed and broken during simulated indentation (Fig. 4 and Supporting Information Figs. S5 and S6). The experiment is different from our simulations in several ways. Specifically, the geometry of the simulation and the kinking is probably different because it is likely that several PFs are already broken by katanin in order to observe any kinking at all. Next, we cannot control the number of PFs that remain continuous in kinking experiments. It is the number of PFs connected that likely gives the filament enough flexibility to be thermally fluctuated. Finally, the number of PFs connected is changing over time due to the breakage of PFs from katanin activity and fluctuations.

As detailed in Section I.6 from the Supporting Information, to account for the effect of the differences in length-scales between experimental and computational filaments, the experimental data should be compared with data from simulations of lattices with both ends fixed to mimic the constraints that exist in the experiment. We observe a striking correlation between the distributions of experimentally measured, macroscopic kinking angles and the simulated, local kinking angles (Fig. 5). In particular, we observe the CDFs for our indentation runs of MT lattices with 2% defects and both ends fixed and the one from our 100 nM katanin experiments are very similar statistically. Given that we polymerize our MTs quickly at high temperature and high tubulin concentration prior to stabilizing with Taxol, it is perhaps not surprising that we would have a high incidence of defects. Further, our current measurements from in vitro experiments closely recapitulate the kinking angles previously measured in Fig. 4A in Davis et al. [Davis et al., 2002]. Future experiments and models of the example situation of kinking MTs could be performed to test these differences exactly.

## Distributions of Breaking and Recovery Times Indicate How Defect-Free MT Filaments Are Protected Against Mechanical Damage

In our indentation simulations, we found that the average time (in frames) required to first break inter-dimer contacts in the lattice is highest for the defect-free AHM and regular lattices and shortest for lattices with two missing dimers (Fig. 6). Namely, the defect-free lattice requires, on average, force application for twice as long of time, i.e., 10 ms (or $249 \pm 32$ frames) to experience damage compared to lattices with defects composed of 2 missing dimers, i.e., 6 ms (or $154 \pm 34$ frames). This result aligns very well with the experimental result [Schaedel et al., 2015] that MTs with minimal lattice defects, do not show any sign of damage

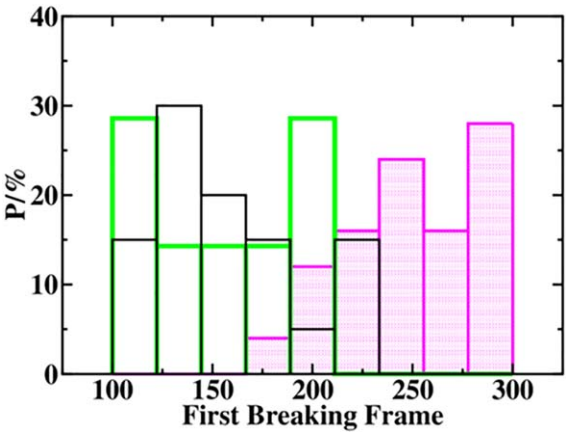


**Fig. 6. Distributions of the frame corresponding to the first breaking event.** We show data for the 3 categories of MT lattices in simulations: defect-free (magenta, 25 points), MT with 1 defect under the tip (green, 14 points) and MT with 2 defects under the tip (black, 20 points). The K-S statistical similarity test applied to the corresponding CDFs indicates that the two data sets for defects are dissimilar from the defect-free one ($D_{crit} = 0.608$, $D$(magenta,green) = 4.2, $D$(magenta,black) = 4.1), while being similar to each other ($D$(green,black) = 0.471). [Color figure can be viewed at wileyonlinelibrary.com]

when exposed briefly to hydrodynamic flow, while lattices with defects experience increased damage upon flow.

Thery and coworkers [Schaedel et al., 2015] investigated the ability of the MT lattice to recover after bending under flow applied for a set time (10 s). They monitored the recovery by allowing the filaments to rest for increasing amounts of time after bending and concluded that even MTs with defects are able to recover after the longest rest period probed in their experiments [Schaedel et al., 2015]. We can do the same in our simulations. Above, we allowed MTs to rest for long time periods (up to 50 ms or $\sim$ 1250 frames) after pushing. Next, we investigated the dependence of the lattice recovery on the duration of the force application. We varied the force time between 194 frames (7.8 ms) and 410 indentation frames (16.4 ms) (Supporting Information Tables S4 and S5) for the defect-free cases and lattices with defects. Importantly, in all our runs we started retraction only after at least two dimers exhibited broken inter-dimer interfaces.

We found that the total time required for the defect-free lattice to recover after initial damage (retraction after a set number of frames of indentation) is the shortest among all types of lattices probed in our study (Supporting Information Tables S4 and S5, and Fig. S9). That is, for recovery started after at most 250 indentation frames it takes on average 111 frames for the defect-free lattice to recover. For filaments with one missing dimer, the average recovery is 149, and for 2 missing dimers it is 206.

For recovery started after 250 to 300 frames it takes on average 175 frames for the defect-free lattice to recover, while for the lattice with a missing dimer the average is 220, and for the lattice with 2 missing dimers the average exceeds 227 (as 2 trajectories out of 4 did not recover). For recovery started after 300 to 360 indentation frames it takes the defect-free lattice on average 150 frames to recover, while the average is 286 for the lattice with 1 missing dimer and 331 for the lattice with 2 missing dimers. Finally, for the recovery started after 360 to 410 indentation frames it takes the defect-free lattice on average more than 400 frames for recovery (because some runs do not recover), while the average far exceeds 500 frames for the lattices with defects (as only one of the runs leads to recovery within 500 frames). Thus, the longer we push to break the lattice, the longer recovery takes.

Comparing the different lattice types, we found that the AHM lattice is the most resistant to damage. For instance, retraction started from frame 260 in the regular lattice pushing between PFs with both ends fixed corresponding to 2 broken dimers recovers in 200 frames, while retraction started from frame 295 in the AHM lattice pushing between PFs with both ends fixed corresponding to 3 broken dimers recovers in 51 frames (Supporting Information Table S4).

## Role of Correlations between Changes in Dimer Contacts in Driving the Recovery of the Lattice

To gain insight into the factors that allow the lattice to recover, we focused on measuring the degree of correlated changes in the positions of the broken subunits. Following the approach described in the Section I.4 from the Supporting Information, we determined the correlations between the time series of the contacts at dimer-dimer interfaces that were broken during the indentation phase. We found that recovery occurs when there are no anti-correlations between any pair of dimers. Secondly, one or more of the following has to happen: (1) the correlations between the recovery of lateral contacts in pairs of dimers which are neighbors along a PF are very high ($\sim$ 0.90); (2) the correlations between the recovery of longitudinal contacts in pairs of dimers which are neighbors along a PF are very high ($\sim$ 0.90); (3) the correlations between the evolution of the overall contacts in pairs of dimers which are neighbors in a ring located right under the cantilever tip are virtually 1 (for recovery after pushing on a PF); (4) the correlations between the evolution of longitudinal contacts in at least one pair of dimers which are neighbors in a ring located under the tip is high (for recovery after pushing between PFs).

In contrast, a lack of full recovery to the original, intact, state of the filament was characterized by either the presence of at least one anti-correlated evolution of contacts in neighboring dimers or by a lack of correlation (correlation coefficient $< 0.20$) between the time series of contacts in any neighboring dimers that had been broken during

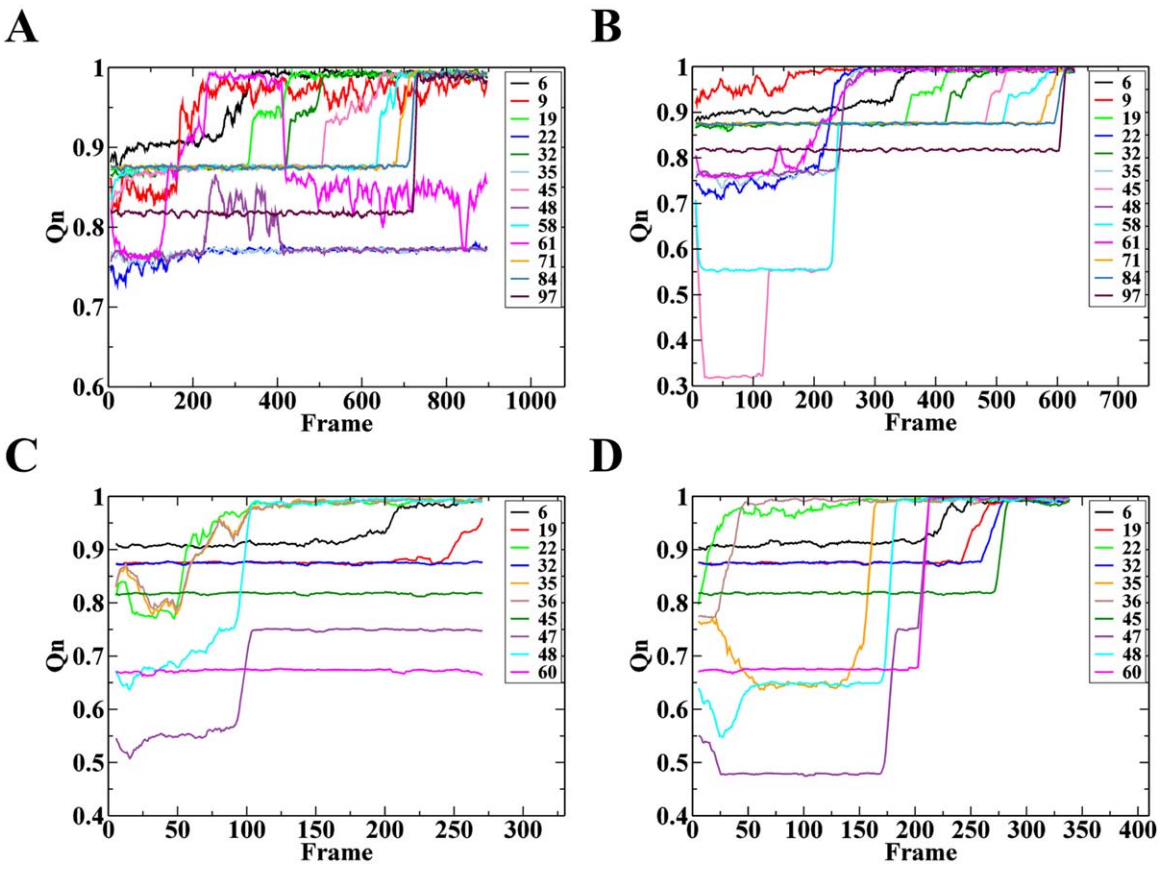


**Fig. 7.** Contacts vs. frame curves for 4 different retraction simulations started from the 2 indentation runs depicted in Supporting Information Figs. S10 and S11. The labels represent the individual dimers that break during the indentation among the 104 dimers, numbered according to Supporting Information Fig. S1. (A): Retraction for the defect-free regular MT with plus end free with plane starting from indentation frame 395 in Supporting Information Fig. S10A and S11A. The lattice does not fully recover. (B): Retraction for the defect-free regular MT with plus end free starting from the same indentation frame as in (A), but without the plane. The lattice recovers fully. (C): Retraction for the MT with missing dimers 58 and 59 with both ends fixed and with plane, started from indentation frame 297 in Supporting Information Figs. S10B and S11B. The lattice does not recover. (D): Retraction for the MT with 58 and 59 missing starting from the same indentation frame as in (C), but with the plus end free and without the plane. The lattice recovers fully. [Color figure can be viewed at wileyonlinelibrary.com]

indentation. To illustrate this principle, the retraction in the lattice with 2 lateral missing dimers (dimers 58, 59) depicted in Figure 7C, when the filament does not recover fully, is an example. We found that the correlation coefficients for neighboring dimers in PF 6 and in the fourth ring starting from the minus end of the filament are all virtually zero (see Supporting Information Fig. S1 for PF numbering). However, for the retraction in the same type of lattice, but now in the absence of constraints, depicted in Fig. 7D, where the filament recovers fully, we found that the correlation coefficients for neighboring dimers in PF 6, as well as the correlation coefficient for the time series of native contacts formed by dimers 44 and 45 from the fourth ring, are all $\sim$ 0.90. In summary, our data strongly suggests that a correlated recovery of the native interface contacts formed by dimers which are neighbors along a PF is the primary factor that accounts for a complete recovery of the intact structure of a MT after breaking.

## Role of Environmental Constraints in the Collapse and Recovery of MT Filaments

Often the presence of the plate used in the AFM force experiments and in our simulations which mimic this setup has no effect on either the critical force or on the indentation pathway (see Supporting Information Tables S1–S3). In contrast, the plane is often inhibitory for recovery of the original lattice structure. In many cases where there is no full recovery of the original MT structure, restarting the retraction from the same indentation frame but eliminating the plane allows for the full recovery of the filament (see Supporting Information Tables S4 and S5 for details). This is seen for example, in the behavior of the normalized contacts, $Q_n$ (the ratio between the number of contacts during the simulation versus the number for the native state of the MT lattice), for the broken interfaces of a defect-free MT lattice with its plus end free after pushing between PFs with retraction starting at frame 395 of the indentation run (depicted in Supporting Information Figs. S10A and S11A

and shown in Movie S2) with the plate (Fig. 7A) and without plate (Fig. 7B). The MT without the plate recovers completely in 610 frames (see Supporting Information Movie S3), while in the MT with the plate has three interfaces that are still broken at the end of the retraction run (after 1000 frames).

There is a second type of constraint which plays a role in the recovery: the state of the ends of the filament. Allowing the plus end to fluctuate freely is usually beneficial for recovery upon retraction (see Supporting Information Table S4). This is seen for example in the case of the retraction for the AHM lattice after pushing between PFs for 380 frames (see the indentation/retraction curve in Supporting Information Fig. S11C and the contacts evolution in Supporting Information Fig. S12A). This system recovered fully (in 181 frames) only when we eliminated the constraints at the plus end of the filament (Supporting Information Fig. S12C); if we keep both ends fixed, 3 of the 8 broken dimers do not recover even after $\sim$ 350 frames of run (Supporting Information Fig. S12B). Interestingly, we found that the lack of recovery when both ends are fixed is due to an increase in the length of the MT fragments that break longitudinally such that upon retraction they can no longer fit together in a straight line leading to the formation of a permanent dislocation in the filament structure. The increase in the length of a fragment is usually due to the relaxation of a couple of dimers at the newly formed end. Only the release of the constraint at an end of the lattice can accommodate the change in length to the degree that upon retraction the two fragments can be properly united along the straight backbone of the lattice.

Furthermore, the recovery pathways, in the presence or absence of constraints are different. This is seen in the case of the MT lattice with dimers 58,59 missing and forced applied between PFs, which follows pathway P11 (with $Q_n$ evolution in Supporting Information Fig. S10B and shown in Supporting Information Movie S4). When we started the retraction from the frame 297 of the indentation (dashed cyan line in Supporting Information Fig. S10B), we found that in the presence of the plate there is no recovery (Fig. 7C), as depicted in Supporting Information Movie S5. However, when we removed both the plate and the constraints placed on the plus end of the filament, all 10 broken dimer interfaces reform in 279 frames (see Fig. 7D and Supporting Information Movie S6). With the plate and both ends fixed, the first dimer recovers after 76 frames, while dimers 36, 47, and 48 showed at least partial recovery around frame 100. Without the plate and with the plus end free, dimers 36, 47, and 48 recovered after 150 frames, even though the first dimer recovers after only 43 frames. There are substantial changes in the correlations between contacts for the various dimers, which, as discussed above, are responsible for the recovery. In protofilament 6 (PF6), correlations between lateral contacts recovery are $c_{lat}$ (19,32) = $c_{lat}$ (32,45) = $c_{lat}$ (71,84) = 0 with the plate, but they all become $\sim$ 0.90 without the plate. The dimers that recover with the plate are, in time order: 22, 35, 36, 48, 47 (only partially), 6, and 19. Without the plate they are: 22, 36, 35, 48, 47, 60, 58, 6, 19, 32, and 45. Thus the delayed reformation of inter-dimer contacts of the MT lattice in the simulation without the plate, compared with the early (partial) formation of contacts in the simulation with the plate (see Fig. 7D versus Fig. 7C), likely accounts for the full recovery of the filament structure in the former case.

## Discussion

Materials made of highly-ordered subunits with pre-existing defects, such as missing subunits, cracks, and dislocations are more likely to fatigue and thus have altered mechanical properties [Landau & Lifshitz, 1986]. It has long been postulated that MT lattices with defects should have altered mechanical properties and also display fatigue. Indeed, this was recently found by Schaedel et al. [Schaedel et al., 2015], using a microfluidic device. Our simulation approach, employing an atomistic representation of the MT lattice allows us to go further by controlling the extent and the position of defects, as well as the location of the force pushing on the filament. We not only show that defects in the lattice lower the force requirements to break the structure, but provide quantitative information about the ratio of force values and reveal the corresponding molecular conformations of MTs during breaking. We also performed the first investigation of the role that constraints placed on the MT play during the breaking and recovery of the filament, which, as discussed below, are important in vivo for example during severing of bundled MTs [Zhang et al., 2013].

In our simulations we found that lattices with defects in the form of subunit vacancies need half or only a third of the maximal force of the defect-free MT to experience such a backbone kink. The force we estimate would correspond to the action of a few tens of katanin motors acting on the lattice [Mohrbach & Kulić, 2007]. Prior AFM indentation experiments [de Pablo et al., 2003; Schaap et al., 2006; Munson et al., 2007; Donhauser et al., 2010] do not discuss pathways of breaking MT structures because they cannot resolve them. Using our results, we posit direct ways to infer pathway variety based on data directly measured in such experiments: force versus indentation curves and critical force distribution. Pathway P3 would be the easiest to detect as in this case the force indentation curve will exhibit only a force plateau (no peak) corresponding to the crushing of the lattice. A force plateau followed by a high critical force peak characterizes P4. While P1 and P2 are more difficult to distinguish, the spread of the critical force distribution is much larger in P2 than in P1 (Supporting Information Table S1). Finally, P12 leads to lower critical forces than P11.

We find excellent correlation between the kinking angles distribution from our simulations of MT lattices with 2% defects and our severing experiments with 100 nM katanin.

This correlation strongly supports the proposed role of lattice defects as binding and/or high activity sites for severing, as previously reported for katanin severing [Davis et al., 2002; Díaz-Valencia et al., 2011]. In our experiments, MTs are grown under high tubulin concentration conditions (45 μM), thus we expect them have a high frequency of lattice defects [Janson & Dogterom, 2004]. If defects are binding sites for severing proteins, then the higher the concentration of severing proteins, the higher the degree of occupancy of these sites and thus the likelihood that severing initiates at such sites. This is exactly what the match between the CDFs of simulations and the 100 nM katanin experiments suggests. These results correlate with our prior results of a concentration-dependence of initiation of katanin severing as a function of added katanin [Bailey et al., 2015].

A non-trivial result emerging from our study is that the MT lattice possesses a double mechanism of protection against damage. First, a defect-free lattice survives the longest before cracking upon indentation. Second, defect-free lattices are able to heal the fastest upon retraction. We see this in the all homogeneous (AHM) lattices that mimic the GTP state. By the same token, lattices with defects (subunit vacancies prior to indentation) face an uphill battle in maintaining their structure under the action of a pushing force. They break easily upon indentation and take a long time to heal upon retraction. The larger the number of defects, the more serious this effect is (Supporting Information Tables S4 and S5).

Usually indentation and retraction follow different routes. Namely, during indentation, bending and buckling of the MT lattice occur first. For retraction the straightening of the PFs occurs last only when we start it after just a few dimers lose contacts. In contrast, when we wait and start retraction after many dimers break interfaces with their neighbors, we observe initial recovery of some of the interfaces, followed by the straightening of the PFs only at the end when the lattice has completely healed the majority of the interfaces. This shows that recovery of broken interfaces is highly dependent on the constraints that defect-free, straight PFs place on their neighbors. This conclusion is based on our finding that lattice recovery is the result of high correlations between the recovery of native contacts in consecutive dimers in a PF, rather than due to correlations between dimers in a ring. This finding supports the idea that the growth of a defect-free MT lattice occurs primarily by addition of subunits longitudinally to a PF and not to lateral neighbors [Ghosh et al., 2012].

Prior experimental work has shown that MTs are more likely to have defects when grown quickly, in conditions of high tubulin concentration [Janson & Dogterom, 2004]. Intuitively, fast addition of new dimers to ends results in lower correlations of growth and more defects. Our results also support the ideas that the plasticity of the MT lattice, which allows it to populate highly bent shapes such as loops or full rings, results from the ability of the PFs to translate versus one another [Pampaloni et al., 2006]. This is exemplified in the indentation pathway P3 detailed above. Further, the dimers within the GDP lattice are in a loaded spring-like state which can be relieved upon removal of the GTP cap [Alushin et al., 2014]. This is observed in the retraction runs with the plus end free.

An unexpected finding is that the local, physical environment has a large effect on healing the lattice, but not on breaking it. For instance, when we include or exclude a base plate during indentation, we observe no effect on either the value of the critical force or the breaking pathway. This result is confirmed by AFM experiments [Schaap et al., 2006; Munson et al., 2007]. Oppositely, for recovery the presence of the plate is inhibitory to healing most of the time. We also observe that fixing both ends of a filament also inhibits healing of the lattice. Specifically, when a couple of PFs break longitudinally in the middle, the dimers in each of the two segments can relax (i.e., expand). Reformation of the longitudinal interfaces is impossible because the lengths of the segments no longer match their original length. This might be an illustration of the proposed failure to incorporate dimers in growing MTs if neighboring PFs add dimers at a faster pace than the middle PF [Chrétien et al., 1992; Schaap et al., 2004]. Such events likely lead to the creation of defects when MTs polymerize quickly [Janson & Dogterom, 2004; Schaedel et al., 2015].

More importantly our results strongly suggest that anchoring the MT lattice, as is done in AFM experiments on a plate and *in vivo*, for instance in MTs from crosslinked networks, is often inhibitory for lattice healing after breakage. The literature reviewed above [Davis et al., 2002; Bailey et al., 2015, 2016] indicates that the action of severing proteins on MTs is not continuous, but experiences pauses, as other AAA+ machines, such as Clp machines [Cordova et al., 2014]. Thus, while it is reasonable to assume that bundled (or otherwise constrained) MTs can be severed more readily than fluctuating MTs, our simulations show that this is not because the plane (or constraint) can help reduce the critical MT breaking force. Instead, it is because once a critical number of dimers is broken (at least 6 in our simulations) the lack of flexibility imposed by the restraints lengthens the recovery time substantially. Thus, the lattice will not have time to heal during the pauses in the action of severing enzymes. On the other hand, freely fluctuating MTs, such as defect-free filaments without constraints would likely be able to recover to their original states when severing proteins pause. Our findings corroborate recent experimental results that katanin preferentially severs at crossover sites in non-centrosomal cortical MTs (CMTs) from plant cells, i.e., at intersections corresponding to growing CMT plus ends crossing over preexisting CMTs [Zhang et al., 2013]. Moreover, just as we would predict from our simulations, this study found a strong bias for longer-lived crossover sites to be severed [Zhang et al., 2013].

Our simulations, due to their systematic and molecular-level detail reveal new information about how best to destroy MT lattices, specifically by applying forces, which severing enzymes presumably do. Our work can inform on currently unknown mechanisms for MT severing action. We can begin to address questions such as: Where do severing enzymes act on MT lattices - on a PF or between PFs [Sharp & Ross, 2012]? Do they apply forces inward, to crush the filaments, as we do here? Or do they apply outward, pulling forces, as we have previously examined [Theisen et al., 2012]? Can we distinguish between two proposed models: the "unfoldase" model and the "wedge" model [Vale, 2000; Roll-Mecak & Vale, 2008; Bailey et al., 2016]?

The unfoldase model postulates that the severing enzyme binds to and pulls on the tubulin carboxy-terminal tail via the 2 nm pore at the center of the AAA+ enzyme hexamer. ATPase activity causes the enzyme to processively translocate along the tubulin polypeptide, pulling the dimer from the lattice via the carboxy-terminal tail. Evidence for this mechanism includes the fact that the carboxy-terminal tail is the target for severing enzymes and is required for severing to occur [McNally & Vale, 1993; White et al., 2007; Roll-Mecak & Vale, 2008]. The unfoldase mechanism is based on the similarities between MT severing enzymes and other unfoldase enzymes, such as ClpX [Baker & Sauer, 2012; Cordova et al., 2014].

The wedge model postulates that the tubulin carboxy terminal tail is the anchor point for the other regions of the AAA+ hexamer to apply inward force pressure to the lattice to break it apart. Evidence for the wedge model includes that fact that 80% of dimers removed by severing are competent to repolymerize into MTs [Roll-Mecak & Vale, 2008]. If tubulin is unfolded by severing enzymes, this would not be possible, since tubulin requires chaperones for correct folding [Llorca et al., 2000]. Other AAA+ enzymes are thought to wedge apart their substrates [Vale, 2000]. Other evidence comes from prior work showing that severing enzymes may sever first at lattice defects [Davis et al., 2002; Díaz-Valencia et al., 2011]. Future studies combining experiment and theory may be able to distinguish these two models.

Here we show that MTs with defects are easier targets for lattice destruction by inward pushing, as might occur in a wedge model. It has been shown that severing enzymes exploit defects to cause MT severing [Davis et al., 2002; Díaz-Valencia et al., 2011]. Taken together, our work indicates that severing enzymes target defects to take advantage of the weak mechanical nature of these regions. This is unlike the proposed mode of action of fluid flow (Fig. 6 in [Schaedel et al., 2015]) where filament bending is a combination of compression and expansion along the lattice - not localized like a severing enzyme would be.

We found that, for defect-free MT lattices, when indentation is applied on a PF after the initial break of lateral contacts the rest of the breaking involves only longitudinal contacts at the interface between the dimers, in rings located under the cantilever sphere. In contrast, indentation between PFs usually leads to an expansion of the lateral crack opened during the first breaking event. As severing requires breaking of longitudinal interfaces, these results suggest that, to sever defect-free MTs, it will be more efficient for severing proteins to act on PFs rather than between them. While for lattices with vacancies under the tip, the pathway to collapse always involves breaking longitudinal interfaces, pushing on a PF leads to only limited further damage of the filament. Large damage, beyond initial defects, appears only when the force is applied between PFs. Thus, if the limiting factor in severing is the extent of damage inflicted on the MT filament in one step, then for lattices with defects it is best if severing proteins act (apply force) between PFs. If the force magnitude is the limiting factor, then acting on a PF is desirable when severing lattices with defects.

Our results are essential to understanding how MTs withstand mechanical forces in cells and the role that defects might have in those processes. Further, recent biological studies have shown that loss of dimers from the MT can be healed and are resistant to depolymerization for a time after healing [Aumeier et al., 2016]. Thus, defects that can recover, as we study here, have downstream effects on MT mechanics, network robustness, and even network remodeling that can affect cell morphology and motility.

## Materials and Methods

### The Potential Energy Function

We used a topology-based model (the self-organized polymer or SOP-model) for the MT lattice in which each amino acid is represented by its $C_\alpha$ atom [Hyeon et al., 2006a]. The total potential energy function for the conformation of the given protein, specified in terms of the coordinates ($r_i$) (i = 1,2, ... N) where N is the total number of residues, is

$$\begin{aligned} V = V_{\mathrm{FENE}} + V_{\mathrm{NB}}^{\mathrm{ATT}} + V_{\mathrm{NB}}^{\mathrm{REP}} = \\ -\sum_{i=1}^{\mathrm{N}-1} \frac{k}{2} R_0^2 \log\left(1 - \frac{\left(r_{i,i+1} - r_{i,i+1}^0\right)^2}{R_0^2}\right) \\ + \sum_{i=1}^{N-3} \sum_{j=i+3}^{N} \epsilon_h \left[\left(\frac{r_{ij}^0}{r_{ij}}\right)^{12} - 2\left(\frac{r_{ij}^0}{r_{ij}}\right)^{6}\right] \Delta_{ij} \\ + \sum_{i=1}^{N-2} \epsilon_r \left(\frac{\sigma}{r_{i,i+2}}\right)^6 + \sum_{i=1}^{N-3} \sum_{j=i+3}^{N} \epsilon_r \left(\frac{\sigma}{r_{ij}}\right)^6 \left(1 - \Delta_{ij}\right) \end{aligned} \quad (1)$$

Here, the distance between two interacting residues $i$ and $i+1$ is $r_{i,i+1}$, and $r_{i,i+1}^0$ is the corresponding value in the native structure. The first term in Eqn.(1) is the backbone chain connectivity potential. The second term accounts for

the non-covalent interactions that stabilize the native (folded) state. If the non-covalently linked residues $i$ and $j$ ($|i - j| > 2$) are within a cut-off distance $R_C$ (i.e., $r_{ij} < R_C = 8\mathring{A}$) $\Delta_{ij} = 1$, and zero otherwise. All non-native interactions, described by the third and fourth terms in Eqn.(1), are treated as repulsive. Also, in this equation $R_0 = 2\mathring{A}$ and $\varepsilon_l = 1$ kcal/mol, following [Hyeon et al., 2006a]. The $\varepsilon_h$ value, which accounts for the strength of the native contacts in the lattice and is the only variable in the above potential energy function, varies according to the type of contacts.

## Parameterization of the SOP-Model

In the regular MT setup, for the intra-dimer contacts we used $\varepsilon_h$ of 1.9 kcal/mol, while for the longitudinal inter-dimer and the lateral inter-dimer we used 1.0 kcal/mol and 0.9 kcal/mol, respectively. These values were determined in our previous work (Supporting Information Table S3 in [Kononova et al., 2014]). Namely, we extracted the values of $\varepsilon_h$ from MD simulations of the atomistic structure model of the MT lattice at $T = 300$ K using two implicit solvent models [Eisenberg & McLachlan, 1985; Ferrara et al., 2002; Im et al., 2003]. Given the orthotropic properties of the MT lattice [VanBuren et al., 2002], we divided all the native contacts into five groups: (1) the intramonomer contacts in α-tubulin; (2) the intramonomer contacts in the β-tubulin; (3) the intradimer contacts that stabilize the dimer's structure; (4) the longitudinal interdimer contacts between any two dimers along a PF; and (5) the lateral interdimer contacts between monomers in adjacent PFs. For each group of contacts, we calculated from the output of the MD simulations the average nonbonded energy (Enb), given by the sum of the van der Waals energy and the electrostatic energy. We also determined the average number of contacts between amino acids that stabilize the native MT structure (Nnb), where each contact satisfied the criterion for the second term in Eqn.(1). The value of $\varepsilon_h$ for each of the five groups of contacts in the regular (GDP-like) MT lattice was the ratio between Enb and the corresponding value of Nnb for the contact group.

The regular lattice (which mimics a GDP state [Kononova et al., 2014]) exhibits a high degree of asymmetry in the strength of lateral contacts between the various PFs and of longitudinal contacts between dimers in a PF. This has also been reported in Fig. 8 from [Ayoub et al., 2015], from full atomic and explicit solvent simulations. In our MT model there are a fairly small number of lateral contacts between PF5 and PF6 and a small number of longitudinal contacts in PF3 (PF numbering listed in Supporting Information Fig. S1). To determine the role of weak interfaces in the indentation/retraction pathways, we created additional MT models with altered distributions of interaction parameters for lateral and/or longitudinal contacts. The first is a PF5-PF6 interface enhanced MT ("PF5-PF6") model. Because the number of contacts in this interface is half of the average, we increased the lateral interaction parameter for PF5-PF6 from 0.9 kcal/mol to 1.8 kcal/mol. The second model is the laterally homogeneous MT (LHM) model, in which all lateral interfaces are adjusted to the same total energy value (equal to the average energy for a lateral interface in the regular MT model). Operationally, for each lateral interface between two adjacent dimers ($L_i$), we assigned a specific $\varepsilon_h$ value per native contact, $\varepsilon_h$ ($L_i$), given by $\varepsilon_h$ ($L_i$) = $N_{lat}/N_i \times 0.9$ kcal/mol, where $N_{lat}$ is the average number of lateral contacts between dimers in the MT lattice, and $N_i$ is the number of such contacts in the given lateral interface. The third model is the all homogeneous MT (AHM) model in which, on top of the condition for the LHM model, all the longitudinal interactions are set to the average energy per longitudinal interface in the regular MT model. Tuszynski and colleagues [Ayoub et al., 2015] found that the GTP-like state of the lattice corresponds to fairly homogeneous energetics of lateral and longitudinal interfaces. Thus, LHM and AHM could be stand ins for the GTP (or GMPCPP)-like state of a MT. Moreover, the rationale to use homogeneous lateral contacts to mimic a rigid (GMPCPP-like) filament [Munson et al., 2007] stems from newly reported MT structures [Alushin et al., 2014; Zhang et al., 2015], which highlighted the differences between the GMPCPP and the GDP lattices. Namely, while the identity of the lateral contacts is the same in the two lattices, they experience different levels of pre-stress based on the nucleotide type: in the GDP lattice there is substantial stress in contacts due to the compaction around the E-site, which likely leads to a non-uniform strength distribution of contacts. In contrast, in the presence of GMPCPP there is no compaction and thus all lateral contacts can be assumed to be of similar strength.

## Mechanical Indentation Set-up

To mimic the experimental set-up from AFM indentation studies [de Pablo et al., 2003], we included a cantilever tip to the MT wall potential and an interaction between the filament and the plate on which it rests [Kononova et al., 2014]. For the tip-MT wall interactions, we used a repulsive Lennard-Jones potential, $V_{LJ} = \varepsilon_{LJ}\,(\sigma_{LR}/(r_i - R_{tip}))^6$, where $\varepsilon_{LJ} = 4.18$ kJ/mol, $\sigma_{LR} = 1.0\mathring{A}$ is the distance between the center of the tip and an amino acid, $r_i$ is position of the $i$-th particle, and $R_{tip} = 10$ nm is the radius of the spherical tip (see Fig. 1). Importantly, the radius of 10 nm is close to the reported size of the diameter of the spastin hexamer [Roll-Mecak & Vale, 2008]. The cantilever spring constant was $k_s = 50$ pN/nm, which is in the AFM experimental range. Following the experimental setup [de Pablo et al., 2003], we constrained one surface of the filament by fixing $C_\alpha$ -atoms along the perimeter (see Supporting Information Fig. S1) to account for the cylinder resting on a plane. The tip exerted a time-dependent force in the direction perpendicular to the longitudinal axis of the filament. We used an

indentation speed $v = 2.0$ μm/s, recalling the experimental value [de Pablo et al., 2003].

## Computational Set-up and Data Analysis

We used two MT lengths: 8 and 12 dimers in each PF, starting from the atomistic structure of the filament [Wells & Aksimentiev, 2010]. The numbering of subunits in the 8 dimers case is in Supporting Information Fig. S1. Moreover, we simulated 8 dimers long lattices with 1% and 2% defects (missing dimers). All simulations were performed using the SOP package implemented on GPUs [Zhmurov et al., 2010] at T = 300 K. Details of the set-ups, estimation of the integration timestep, and a description of the structures used in simulations are in Sections I.1 to I.3 from the Supporting Information. Information about the number of runs for each indentation scenario is in Supporting Information Table S1 for the defect-free lattices and Supporting Information Tables S2 and S3 for lattices with defects, respectively. For various forward indentation runs, we also ran simulations in the opposite direction, i.e., when the force is decreased linearly to zero following the same regime as for indentation but in reverse to determine the degree to which the MT lattice recovers its original state. Some retractions were run without the plane and/or without the constraints imposed on the plus end of the filament. Information about the number of runs for each retraction is in Supporting Information Tables S4 and S5 for the defect-free lattices and lattices with defects, respectively. Throughout the Results section, a frame represents 0.04 ms, corresponding to 1 million simulation steps. Details about the data analysis, including tracking the time evolution of contacts for dimers, kinking angles for the MT lattice, and statistical correlations are in Section I.4 from the Supporting Information.

## Experimental Procedure

Full experimental methods can be found in Section I.5 from the Supporting Information. The protein purification, MT polymerization and stabilization, and in vitro severing assays were identical to those described recently [Bailey et al., 2015]. The analysis we used to measure kinking angles was based on the analysis described previously [Davis et al., 2002]. We observed the kinking and breaking of individual MTs over time using total internal reflection fluorescence microscopy and used Fiji (ImageJ) to measure the angles for 50 nM and 100 nM katanin (see Supporting Information Fig. S3 for details).

## Acknowledgments

This work was partially supported in part by a National Science Foundation grant MCB-1412183 to RID and a National Science Foundation grant DMR-143837 to JLR and National Institutes grant R01-GM109909 to David Sharp (Albert Einstein College of Medicine) and JLR.

## References

Ahmad FJ, Yu W, McNally FJ, Baas PW. 1999. An essential role for katanin in severing microtubules in the neuron. J Cell Biol 145: 305–315.

Alushin GM, Lander GC, Kellogg EH, Zhang R, Baker D, Nogales E. 2014. High-resolution microtubule structures reveal the structural transitions in αβ-tubulin upon GTP hydrolysis. Cell 157:1117–1129.

Aumeier C, Schaedel L, Gaillard J, John K, Blanchoin L, Théry M. 2016. Self-repair promotes microtubule rescue. Nat Cell Biol 18: 1054–1064.

Ayoub AT, Klobukowski M, Tuszynski JA. 2015. Detailed per-residue energetic analysis explains the driving force for microtubule disassembly. PLoS Comput Biol 11:e1004313.

Bailey ME, Jiang N, Dima RI, Ross JL. 2016. Invited review: microtubule severing enzymes couple atpase activity with tubulin GTPase spring loading. Biopolymers 105:547–556.

Bailey ME, Sackett DL, Ross JL. 2015. Katanin severing and binding microtubules are inhibited by tubulin carboxy tails. Biophys J 109:2546–2561.

Baker TA, Sauer RT. 2012. ClpXP, an ATP-powered unfolding and protein-degradation machine. Biochim Biophys Acta 1823:15–28.

Brangwynne CP, MacKintosh FC, Kumar S, Geisse NA, Talbot J, Mahadevan L, Parker KK, Ingber DE, Weitz DA. 2006. Microtubules can bear enhanced compressive loads in living cells because of lateral reinforcement. J Cell Biol 173:733–741.

Chrétien D, Metoz F, Verde F, Karsenti E, Wade RH. 1992. Lattice defects in microtubules: protofilament numbers vary within individual microtubules. J Cell Biol 117:1031–1040.

Chu JW, Voth GA. 2006. Coarse-grained modeling of the actin filament derived from atomistic-scale simulations. Biophys J 90:1572–1582.

Cordova JC, Olivares AO, Shin Y, Stinson BM, Calmat S, Schmitz KR, Aubin-Tam ME, Baker TA, Lang MJ, Sauer RT. 2014. Stochastic but highly coordinated protein unfolding and translocation by the ClpXP proteolytic machine. Cell 158:647–658.

Davis LJ, Odde DJ, Block SM, Gross SP. 2002. The importance of lattice defects in katanin-mediated microtubule severing in vitro. Biophys J 82:2916–2927.

Díaz-Valencia JD, Morelli MM, Bailey M, Zhang D, Sharp DJ, Ross JL. 2011. Drosophila katanin-60 depolymerizes and severs at microtubule defects. Biophys J 100:2440–2449.

Dogterom M, Yurke B. 1997. Measurement of the force-velocity relation for growing microtubules. Science 278:856–860.

Donhauser ZJ, Jobs WB, Binka EC. 2010. Mechanics of microtubules: effects of protofilament orientation. Biophys J 99:1668–1675.

Eisenberg D, McLachlan AD. 1985. Solvation energy in protein folding and binding. Nature 319:199–203.

Feig M, Sugita Y. 2013. Reaching new levels of realism in modeling biological macromolecules in cellular environments. J Mol Graph Model 45:144–156.

Ferrara P, Apostolakis J, Caflisch A. 2002. Evaluation of a fast implicit solvent model for molecular dynamics simulations. Proteins 46:24–33.

Ghosh DK, Dasgupta D, Guha A. 2012. Models, regulations, and functions of microtubule severing by katanin. ISRN Mol Biol 2012:596289.

Humphrey W, Dalke A, Schulten K. 1996. VMD: visual molecular dynamics. J Mol Graph 14:33–38.

Hyeon C, Dima RI, Thirumalai D. 2006a. Pathways and kinetic barriers in mechanical unfolding and refolding of RNA and proteins. Structure 14:1633–1645.

Hyeon C, Lorimer GH, Thirumalai D. 2006b. Dynamics of allosteric transitions in GroEL. Proc Natl Acad Sci USA 103:18939–18944.

Hyeon C, Onuchic JN. 2007. Internal strain regulates the nucleotide binding site of the kinesin leading head. Proc Natl Acad Sci USA 104:2175–2180.

Im W, Lee MS, Brooks CL. 2003. Generalized born model with a simple smoothing function. J Comput Chem 24:1691–1702.

Janson ME, Dogterom M. 2004. A bending mode analysis for growing microtubules: evidence for a velocity-dependent rigidity. Biophys J 87:2723–2736.

Johnson CP, Tang H-Y, Carag C, Speicher DW, Discher DE. 2007. Forced unfolding of proteins within cells. Science 317:663–666.

Kononova O, Kholodov Y, Theisen KE, Marx KA, Dima RI, Ataullakhanov FI, Grishchuk EL, Barsegov V. 2014. Tubulin bond energies and microtubule biomechanics determined from nanoindentation in silico. J Am Chem Soc 136:17036–17045.

Kononova O, Snijder J, Brasch M, Cornelissen J, Dima RI, Marx KA, Wuite GJ, Roos WH, Barsegov V. 2013. Structural transitions and energy landscape for Cowpea Chlorotic Mottle Virus capsid mechanics from nanomanipulation in vitro and in silico. Biophys J 105:1893–1903.

Landau LD, Lifshitz EM. 1986. Theory of Elasticity. Burlington, MA: Elsevier Ltd.

Liu Z, Reddy G, O'Brien EP, Thirumalai D. 2011. Collapse kinetics and chevron plots from simulations of denaturant-dependent folding of globular proteins. Proc Natl Acad Sci U S A 108:7787–7792.

Llorca O, Martín-Benito J, Ritco-Vonsovici M, Grantham J, Hynes GM, Willison KR, Carrascosa JL, Valpuesta JM. 2000. Eukaryotic chaperonin CCT stabilizes actin and tubulin folding intermediates in open quasi-native conformations. Embo J 19:5971–5979.

Maximova T, Moffatt R, Ma B, Nussinov R, Shehu A. 2016. Principles and overview of sampling methods for modeling macromolecular structure and dynamics. PLoS Comput Biol 12:e1004619.

McNally FJ, Vale RD. 1993. Identification of katanin, an ATPase that severs and disassembles stable microtubules. Cell 75:419–429.

Mohrbach H, Kulić IM. 2007. Motor driven microtubule shape fluctuations: force from within the lattice. Phys Rev Lett 99:218102.

Munson KM, Mulugeta PG, Donhauser ZJ. 2007. Enhanced mechanical stability of microtubules polymerized with a slowly hydrolyzable nucleotide analogue. J Phys Chem B 111:5053–5057.

Nogales E, Downing KH, Amos LA, Löwe J. 1998. Tubulin and FtsZ form a distinct family of GTPases. Nat Struct Mol Biol 5:451–458.

de Pablo PJ, Schaap IA, MacKintosh FC, Schmidt CF. 2003. Deformation and collapse of microtubules on the nanometer scale. Phys Rev Lett 91:098101.

Pampaloni F, Lattanzi G, Joná \vs A, Surrey T, Frey E, Florin E-L. 2006. Thermal fluctuations of grafted microtubules provide evidence of a length-dependent persistence length. Proc Natl Acad Sci 103:10248–10253.

Paul R, Heil P, Spatz JP, Schwarz US. 2008. Propagation of mechanical stress through the actin cytoskeleton toward focal adhesions: model and experiment. Biophys J 94:1470–1482.

Reddy G, Liu Z, Thirumalai D. 2012. Denaturant-dependent folding of GFP. Proc Natl Acad Sci U S A 109:17832–17838.

Roll-Mecak A, Vale RD. 2008. Structural basis of microtubule severing by the hereditary spastic paraplegia protein spastin. Nature 451:363–367.

Scarabelli G, Grant BJ. 2013. Mapping the structural and dynamical features of kinesin motor domains. PLoS Comput Biol 9:e1003329.

Schaap IA, Carrasco C, de Pablo PJ, MacKintosh FC, Schmidt CF. 2006. Elastic response, buckling, and instability of microtubules under radial indentation. Biophys J 91:1521–1531.

Schaap IA, de Pablo PJ, Schmidt CF. 2004. Resolving the molecular structure of microtubules under physiological conditions with scanning force microscopy. Eur Biophys J 33:462–467.

Schaedel L, John K, Gaillard J, Nachury MV, Blanchoin L, Théry M. 2015. Microtubules self-repair in response to mechanical stress. Nat Mater 14:1156–1163.

Sharp DJ, Ross JL. 2012. Microtubule-severing enzymes at the cutting edge. J Cell Sci 125:2561–2569.

Theisen KE, Desai NJ, Volski AM, Dima RI. 2013. Mechanics of severing for large microtubule complexes revealed by coarse-grained simulations. J Chem Phys 139:121926.

Theisen KE, Zhmurov A, Newberry ME, Barsegov V, Dima RI. 2012. Multiscale modeling of the nanomechanics of microtubule protofilaments. J Phys Chem B 116:8545–8555.

Vale RD. 2000. AAA proteins. Lords of the ring. J Cell Biol 150: F13–F19.

VanBuren V, Odde DJ, Cassimeris L. 2002. Estimates of lateral and longitudinal bond energies within the microtubule lattice. Proc Natl Acad Sci U S A 99:6035–6040.

Waterman-Storer CM, Salmon ED. 1997. Actomyosin-based retrograde flow of microtubules in the lamella of migrating epithelial cells influences microtubule dynamic instability and turnover and is associated with microtubule breakage and treadmilling. J Cell Biol 139:417–434.

Wei G, Xi W, Nussinov R, Ma B. 2016. Protein ensembles: how does nature harness thermodynamic fluctuations for life? the diverse functional roles of conformational ensembles in the cell. Chem Rev 116:6516–6551.

Wells DB, Aksimentiev A. 2010. Mechanical properties of a complete microtubule revealed through molecular dynamics simulation. Biophys J 99:629–637.

White SR, Evans KJ, Lary J, Cole JL, Lauring B. 2007. Recognition of C-terminal amino acids in tubulin by pore loops in Spastin is important for microtubule severing. J Cell Biol 176:995–1005.

Zhang R, Alushin GM, Brown A, Nogales E. 2015. Mechanistic origin of microtubule dynamic instability and its modulation by EB proteins. Cell 162:849–859.

Zhang Q, Fishel E, Bertroche T, Dixit R. 2013. Microtubule severing at crossover sites by katanin generates ordered cortical microtubule arrays in Arabidopsis. Curr Biol 23:2191–2195.

Zhang Z, Thirumalai D. 2012. Dissecting the kinematics of the kinesin step. Structure 20:628–640.

Zhmurov A, Brown AE, Litvinov RI, Dima RI, Weisel JW, Barsegov V. 2011. Mechanism of fibrin(ogen) forced unfolding. Structure 19:1615–1624.

Zhmurov A, Dima RI, Kholodov Y, Barsegov V. 2010. SOP-GPU: accelerating biomolecular simulations in the centisecond timescale using graphics processors. Proteins 78:2984–2999.

Zhou J, Thorpe IF, Izvekov S, Voth GA. 2007. Coarse-grained peptide modeling using a systematic multiscale approach. Biophys J 92: 4289–4303.